Future trends in upper-atmospheric shear instability from climate change

de Medeiros, J. and Williams, P. D. ORCID: https://orcid.org/0000-0002-9713-9820 (2025) Future trends in upper-atmospheric shear instability from climate change. Journal of the Atmospheric Sciences, 82 (11). pp. 2375-2392. ISSN 1520-0469 doi: 10.1175/JAS-D-24-0283.1 Available at https://centaur.reading.ac.uk/124043/

Future Trends in Upper-Atmospheric Shear Instability from Climate Change

JOANA DE MEDEIROS[a] AND PAUL D. WILLIAMS[a]

[a] *University of Reading, England, United Kingdom*

(Manuscript received 20 December 2024, in final form 13 June 2025, accepted 14 August 2025)

ABSTRACT: Understanding how jet streams respond to a warming climate is crucial for anticipating changes in atmospheric circulation and their broader impacts. Previous studies have highlighted the influence of anthropogenic warming on the meridional temperature gradient, which directly affects jet stream dynamics and variability. This study investigates projected trends in upper-level jet stream shear instability under future climate change scenarios using CMIP6 multimodel simulations. Building on previous findings linking anthropogenic warming to strengthened meridional temperature gradients, we analyze annual means of zonal wind speed, vertical wind shear, and stratification profiles from 2015 to 2100 globally. Results show strengthened multimodel annual-mean vertical shear at 250 hPa, particularly in high-emission scenarios, with trends ranging from 0.04 to 0.11 m s^{-1} (100 hPa)$^{-1}$ decade^{-1} depending on the scenario and region, equivalent to a total relative increase of 16%–27% over 86 years. Decreasing trends are observed in the annual-mean Brunt–Väisälä frequency N^2 at 250 hPa, with multimodel ensemble mean values across regions ranging from -0.018 to -0.040×10^{-4} s^{-2} decade^{-1} for lower and higher emission scenarios, respectively, equating to a total relative decrease of 10%–20%. Similarly, the annual-mean Richardson number Ri shows decreasing trends from -0.014 to -0.050 decade^{-1} across emission scenarios and regions, which is a total relative decrease of 38%–47%. These findings suggest more favorable conditions for the generation of clear-air turbulence (CAT), posing critical challenges for aviation safety and operations in a warming climate.

KEYWORDS: Turbulence; Jets; Stability; Upper troposphere; Climate change; Climate models

1. Introduction

Climate change is increasingly recognized as a major factor influencing atmospheric dynamics, particularly through its impact on the meridional temperature gradient and the variability of the jet stream, especially in midlatitudes (Williams and Joshi 2013; Williams 2017; Lee et al. 2019). These changes have profound implications for aviation safety, as upper-level winds play a critical role in determining flight efficiency and safety (Williams 2016; Simpson 2016; Kim et al. 2016). Optimizing flight paths based on the jet stream's position can help reduce travel time and fuel consumption (Sridhar et al. 2011), but the increased risk of turbulence associated with jet stream variability poses a significant challenge. In fact, turbulence accounts for over 70% of weather-related aviation accidents, leading to substantial financial costs for airlines due to injuries and compensation claims (Gultepe et al. 2019; Sharman and Lane 2016).

The potential for turbulence is particularly high at typical cruising altitudes of around 33 000–42 000 ft, where strong wind and temperature gradients near the jet stream heighten the risk (Jaeger and Sprenger 2007; Karnauskas et al. 2015; Williams and Joshi 2013). This vulnerability is exacerbated when passengers and crew are unbuckled, further increasing the likelihood of turbulence-related injuries (Sharman et al. 2006).

The variability of the jet stream is closely tied to changes in the thermal structure of the troposphere (Palmén 1948), as the distribution of temperature directly influences its position and intensity. However, anthropogenic climate change modifies these dynamics by altering temperature gradients, leading to shifts in jet stream behavior and further complicating its response to atmospheric changes (Williams 2017). For example, in the Northern Hemisphere's lower troposphere, Arctic amplification weakens the meridional gradient and the polar jet stream, while in the upper troposphere and lower stratosphere, polar cooling and tropical warming strengthen the gradient through water vapor feedbacks (Barnes and Screen 2015; Francis et al. 2017; Strong and Davis 2007). This vertical difference creates an interaction in the thermal wind response, where changes in vertical wind shear may provide clearer insights into jet stream trends (Karnauskas et al. 2015). Understanding these dynamics is crucial for refining turbulence forecasting methodologies and improving aviation safety.

A critical factor in linking jet stream variability to turbulence is the Richardson number Ri, which quantifies the balance between buoyancy and shear forces. When vertical wind shear strengthens, Ri can drop below a critical threshold, triggering turbulence. Numerous studies have demonstrated that variations in jet stream structure can lead to such reductions in Ri and initiate turbulence through different mechanisms, including shearing instabilities and gravity wave breaking (Lane et al. 2004; Kim and Chun 2010; Kim et al. 2014; Trier et al. 2022; Lee et al. 2025). These processes may generate Kelvin–Helmholtz instabilities and further destabilize the flow, particularly in regions of enhanced vertical shear and near-cloud environments. Gravity waves can also play a role in modulating Ri and amplifying turbulence episodes (Ellrod and Knapp 1992).

Denotes content that is immediately available upon publication as open access.

Corresponding author: Joana de Medeiros, j.medeiros@pgr.reading.ac.uk

Publisher's Note: This article was revised on 23 October 2025 to correct a typographical error in section 3c.

DOI: 10.1175/JAS-D-24-0283.1

TABLE 1. CMIP6 model description: Model, institution, resolution, and number of members, for the period of 2015–2100 and for both SSPs 245 and 585.

Model	Institution	Horizontal resolution	Members
TaiESM1	AS-RCEC (Taiwan)	~1.13° × 1.13°	1
AWI-CM-1-1-MR	AWI (Germany)	~0.5° × 0.5°	1
BCC-CSM2-MR	BCC (China)	~1.1° × 1.1°	1
CAMS-CSM1-0	CAMS (China)	~2.8° × 2.8°	1
CAS-ESM2-0	CAS (China)	~1.1° × 1.1°	1
CanESM5	CCCma (Canada)	~2.8° × 2.8°	1
IITM-ESM	CCCR-IITM (India)	~2.8° × 2.8°	1
CMCC-CM2-SR5	CMCC (Italy)	1.25° × 0.94°	1
ACCESS-ESM1-5	CSIRO (Australia)	~1.9° × 1.3°	1
ACCESS-CM2	CSIRO-ARCCSS (Australia)	~1.9° × 2.5°	1
MPI-ESM1-2-HR	DKRZ (Germany)	0.9375° × 0.9375°	1
MPI-ESM1-2-LR	MPI-M (Germany)	~1.9° × 1.9°	1
E3SM-1-1	E3SM Project (United States)	~1.0° × 1.0°	1
FIO-ESM-2-0	FIO-QLNM (China)	~1.0° × 1.0°	1
INM-CM5-0	INM (Russia)	~2.0° × 1.5°	1
IPSL-CM6A-LR	IPSL (France)	2.5° × 1.25°	1
KIOST-ESM	KIOST (South Korea)	~1.0° × 1.0°	1
MIROC6	MIROC (Japan)	1.41° × 1.41°	1
MRI-ESM2-0	MRI (Japan)	~1.1° × 1.1°	1
NESM3	NUIST (China)	~1.9° × 1.9°	1
NorESM2-LM	NCC (Norway)	~2.5° × 1.9°	1
GFDL-CM4	NOAA-GFDL (United States)	~1.0° × 1.0°	1
HadGEM3-GC31-LL	MOHC (United Kingdom)	~1.25° × 0.83°	4

Building on the work of Lee et al. (2019), who identified an increase in the annual-mean jet stream vertical wind shear at 250 hPa from 1979 to 2017 in reanalysis data, we extend this analysis to explore how these shifts might evolve under future climate scenarios. This observed increase, driven by changes in the meridional temperature gradient from anthropogenic climate change (Vallis et al. 2015), highlights the importance of understanding how jet streams will respond to a warming world.

Our research aims to assess trends in annual-mean vertical wind shear in the upper troposphere and lower stratosphere (UTLS), both globally and across specific latitude bands. By examining the adjustment of the meridional temperature gradient to global warming, we seek to better understand the structural changes occurring within jet streams (Williams 2016; Woollings et al. 2012). These changes are expected to have significant implications for turbulence, which is closely tied to jet stream variability. For this reason, we also examine annual-mean trends in the Brunt–Väisälä frequency N^2 and Richardson number Ri at 250 hPa, both of which are crucial for understanding the development of clear-air turbulence (CAT) events (Sharman and Pearson 2017; Sharman et al. 2014).

A deeper understanding of jet stream behavior is essential for meteorologists to anticipate shifts in turbulence patterns. Vertical wind shear diagnostics have proven effective for turbulence forecasting, largely due to advances in jet stream dynamics (Colson and Panofsky 1965; Ellrod and Knapp 1992). Despite numerous studies documenting increases in atmospheric turbulence in recent decades and future projections (Williams 2017; Storer et al. 2017; Smith et al. 2023; Williams and Storer 2022; Prosser et al. 2023), long-term trends in jet stream behavior and its role in turbulence in the context of climate change remain underexplored.

To address this gap, we use multimodel outputs from the Coupled Model Intercomparison Project phase 6 (CMIP6) to project potential changes in vertical wind shear and Ri under future climate conditions. This study aims to provide new insights into the evolving dynamics of the jet stream and its broader implications for climate and weather phenomena.

2. Methodology

a. *CMIP6 model data description*

We employ climate model simulations from CMIP6 to study the projected impacts of future greenhouse gas emissions on vertical shear instabilities around the jet stream core. Data from 26 general circulation models (GCMs) were used under two shared socioeconomic pathways (SSPs), SSP2-4.5 (SSP 245) and SSP5-8.5 (SSP 585), representing intermediate and high-emission scenarios, respectively.

These models were selected based on the availability of monthly wind, temperature, and geopotential output, which are required for computing vertical wind shear, static stability, and the Richardson number Ri in the troposphere. The selection also considered model participation in the Scenario Model Intercomparison Project (ScenarioMIP) and the provision of long-term continuous output necessary for trend analysis. While intermodel variability in simulating different turbulence mechanisms [e.g., CAT, mountain-wave turbulence (MWT), near-cloud turbulence (NCT)] is acknowledged (Kim et al. 2023), our focus is on large-scale drivers of CAT and their projected trends under climate change. Table 1 lists the models and relevant output characteristics used in this study.

Additionally, the fidelity of climate models in capturing upper-tropospheric dynamics is central to understanding turbulence changes in a warming climate. Previous evaluations show that CMIP5 models realistically simulate the large-scale characteristics of the Northern Hemisphere jet streams and associated vertical wind shear in a climatological sense (Harvey et al. 2020). CMIP6 models further improve upon CMIP5, notably reducing biases in the position and strength of storm tracks and jet streams, particularly over the North Atlantic and North Pacific (Harvey et al. 2020). These improvements lend confidence to the use of CMIP6 data for assessing long-term trends in jet-related turbulence indicators such as vertical wind shear and the Richardson number.

b. Emission scenarios

We analyzed two SSP scenarios to represent different possible futures. The first, SSP 245, is an intermediate scenario characterized by moderate mitigation and adaptation strategies, leading to a radiative forcing of 4.5 W m^{-2} by 2100. This "middle-of-the-road" pathway reflects a balanced approach to addressing climate change. In contrast, SSP 585 represents a high-emission scenario, assuming continued reliance on fossil fuels with limited climate mitigation efforts. This scenario results in a radiative forcing of 8.5 W m^{-2} by 2100 and reflects a high-end emission trajectory, as described in O'Neill et al. (2016).

c. Data processing

Monthly mean atmospheric variables, including temperature, zonal-mean zonal wind, and geopotential height z_g, were obtained for the period 2015–2100 for the entire globe.

From this dataset, annual means were computed to analyze long-term trends relevant to upper-level tropospheric dynamics. The analysis of vertical wind shear was conducted using two complementary approaches. First, vertical shear was calculated directly from centered differences in the model's zonal-mean zonal wind at adjacent pressure levels. Second, to assess thermal wind balance, vertical shear of the gradient wind [Eq. (1)] was derived and compared to the meridional temperature gradient, following the thermal wind relation that incorporates both Coriolis and centrifugal effects (e.g., Newton and Palmén 1963; Reed and Hardy 1972; Knox 1997) [Eq. (3)]. This dual approach enables a direct quantification of shear alongside a dynamically consistent interpretation of its thermal drivers. For all other diagnostics—including trends in zonal wind, vertical shear, and Richardson number—the model's actual wind fields were used, as they represent the full atmospheric flow and are more relevant for evaluating turbulence risk. Additional diagnostics included the Brunt–Väisälä frequency N^2 [Eq. (4)] which was used in the calculation of the Richardson number. All variables were interpolated onto a common latitude–longitude grid for ensemble mean and spread calculations. Linear trends were computed using least squares regression, with statistical significance evaluated at the 95% confidence level. Correlations were assessed using Pearson's correlation coefficient, also at the 95% confidence level. Statistically significant trends are indicated by stippling (two-tailed t test; $p \leq 0.05$; $n = 86$).

In addition to trend analysis of annual means, we also quantified changes in the right-hand tail of the distribution for each diagnostic to capture shifts in more extreme atmospheric states. The 99th percentile of annual-mean values was calculated for two periods (2015–30 and 2070–2100) across the model ensemble. This method is consistent with the focus of the study on annual-scale variability and trends. The percentage change in the 99th percentile between these periods was then computed for each variable, providing insight into how the more intense expressions of stratification N^2, instability Ri, and vertical wind shear evolve under future climate conditions. This approach complements the mean-state analysis by highlighting projected changes in the frequency and intensity of extreme dynamic environments.

The analysis encompassed the entire globe and several specific regional boxes in both hemispheres. These regions were categorized based on latitude, spanning from the equator to high latitudes. The Northern Hemisphere (NH) and Southern Hemisphere (SH) regions extended from the equator to 70° north and south latitude (0°–70°N/S) across the full longitudinal range (from −180° to 180°). The midlatitude regions [NH midlatitude (NH-M) and SH midlatitudes (SH-M)] covered latitudes between 30° and 70° in both hemispheres (N/S), also spanning all longitudes. Additionally, the tropical regions [NH tropical (NH-T) and SH tropical (SH-T)] were defined between the equator and 30° latitude (0°–30°N/S), with the same global longitudinal coverage.

GRADIENT WIND

To ensure dynamical consistency in the diagnosis of vertical wind shear and its relation to the thermal wind balance, the gradient wind was used in place of model-resolved wind fields. The gradient wind extends the geostrophic approximation by including the centrifugal acceleration due to flow curvature, yielding a more accurate representation of upper-level flow in regions where curvature is significant, such as along the subtropical jet and in midlatitude waveguides (Newton and Palmén 1963; Reed and Hardy 1972; Holton 2004). In height coordinates, the gradient wind balance can be written as

$$\frac{V_{\mathrm{gr}}^2}{R} + fV_{\mathrm{gr}} = -g\,\frac{\partial z_g}{\partial(x,\,y)}, \tag{1}$$

where V_{gr} is the wind speed tangent to the flow, R is the radius of curvature of the flow path (approximated by the curvature of geopotential height contours), f is the Coriolis parameter, g is the gravitational acceleration, and $\partial z_g/\partial(x, y)$ denote the zonal and meridional derivatives of the geopotential height. This formulation enables direct estimation of the balanced wind from geopotential height fields on isobaric surfaces. To compute the curvature radius $R = 1/\kappa$ of the geopotential height, we used a second-order finite-difference approximation based on the geopotential height field $z_g(x, y)$. The curvature is derived from Endlich (1961) and is given by

$$\kappa = \frac{\left[\left(\frac{\partial z_g}{\partial x}\right)^2\left(\frac{\partial^2 z_g}{\partial y^2}\right) - 2\left(\frac{\partial z_g}{\partial x}\right)\left(\frac{\partial z_g}{\partial y}\right)\left(\frac{\partial^2 z_g}{\partial x \partial y}\right) + \left(\frac{\partial z_g}{\partial y}\right)^2\left(\frac{\partial^2 z_g}{\partial x^2}\right)\right]}{\left[\left(\frac{\partial z_g}{\partial x}\right)^2 + \left(\frac{\partial z_g}{\partial y}\right)^2\right]^2}. \tag{2}$$

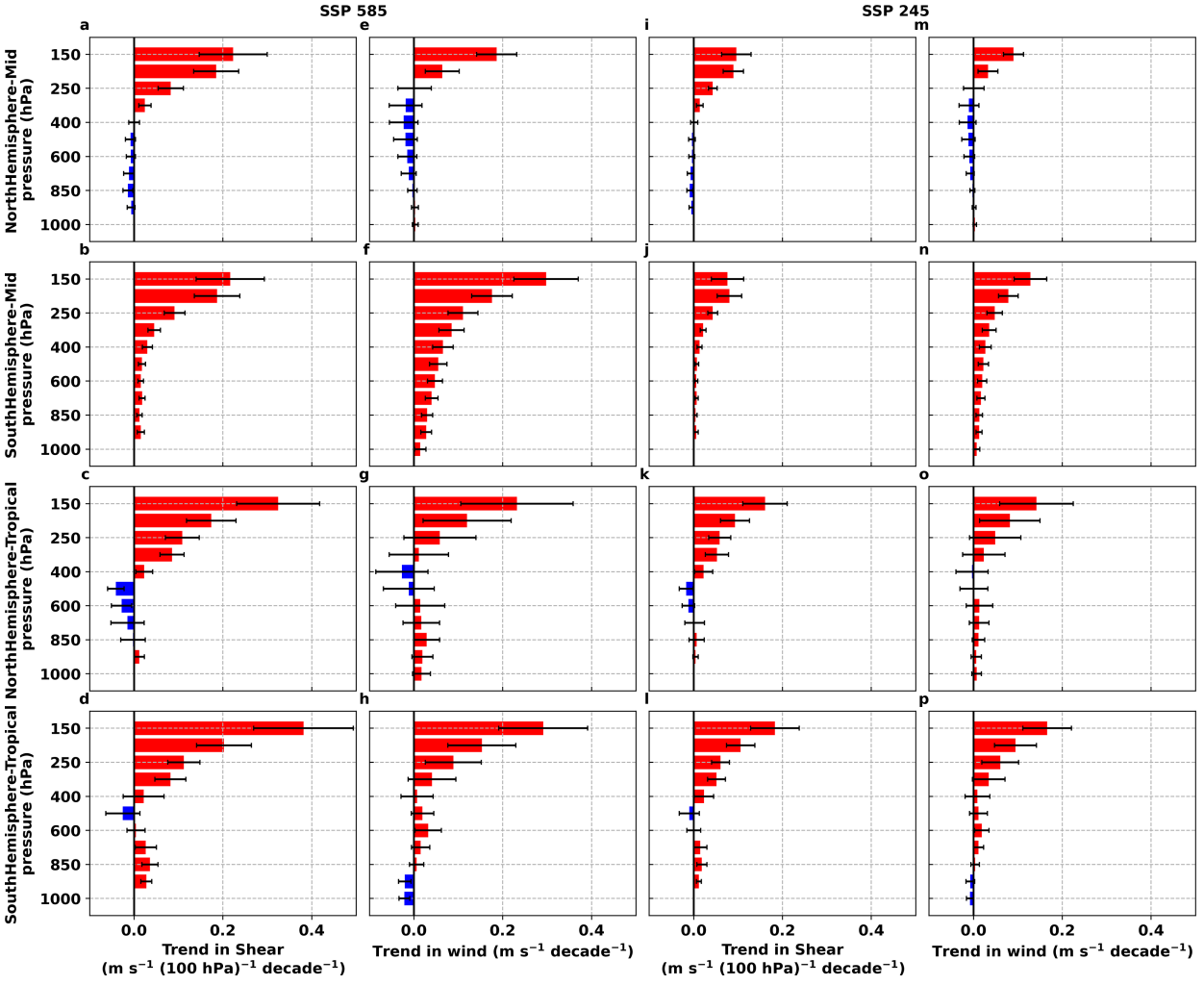

FIG. 1. Vertical profiles of the multimodel mean of annual-mean trends in wind characteristics over the period 2015–2100, shown for four regions (one region per row). (a)–(d),(i)–(l) Trends in vertical shear and (e)–(h),(m)–(p) trends in zonal-mean wind speed, for both (left) SSP 585 and (right) SSP 245 scenarios. Error bars indicate the intermodel standard deviation, representing model spread.

The resulting curvature and gradient were used to solve the gradient wind equation for V_{gr}. Compared to model wind fields, the gradient wind offers a more physically consistent basis for estimating shear and diagnosing the thermal wind balance. This approach follows established theoretical treatments (Holton 2004; Pedlosky 1987; Dutton 1986) and is supported by diagnostic work demonstrating the advantages of gradient-balanced flow in upper-tropospheric dynamics (Knox 1997).

3. Results

a. *Vertical wind shear*

We begin our analysis by looking at the multimodel average trends for the annual-mean zonal wind speeds and the respective vertical wind shear associated with both SSPs over the 86-yr period for the four regions (Fig. 1).

In the NH-M (Fig. 1), for both SSPs, vertical profiles from 1000 hPa exhibit weakly negative mean trends in zonal-mean wind speeds up to approximately 350–300 hPa. However, an increase in zonal wind speed is observed starting near 250 hPa, indicating intensified upper-level jets at these altitudes (Shaw and Miyawaki 2024). Taking centered differences between pressure levels reveals the corresponding vertical wind shear profile, with negative mean trends up to 400 hPa, followed by a significant increase in vertical wind shear from 250 hPa upward. This pronounced increase in shear in the Northern Hemisphere midlatitudes could pose future challenges for aviation, as increased upper-tropospheric turbulence may disrupt flight paths and safety (Williams 2017; Kim et al. 2023). Such trends underscore the impact of projected warming on atmospheric stability and wind patterns, particularly considering polar amplification effects and tropical upper-tropospheric warming (Barnes and Screen 2015; Francis and Vavrus 2015; Francis et al. 2017).

The SH-M band (Fig. 1), however, exhibits a slightly different profile, one of the reasons for which could be attributed to

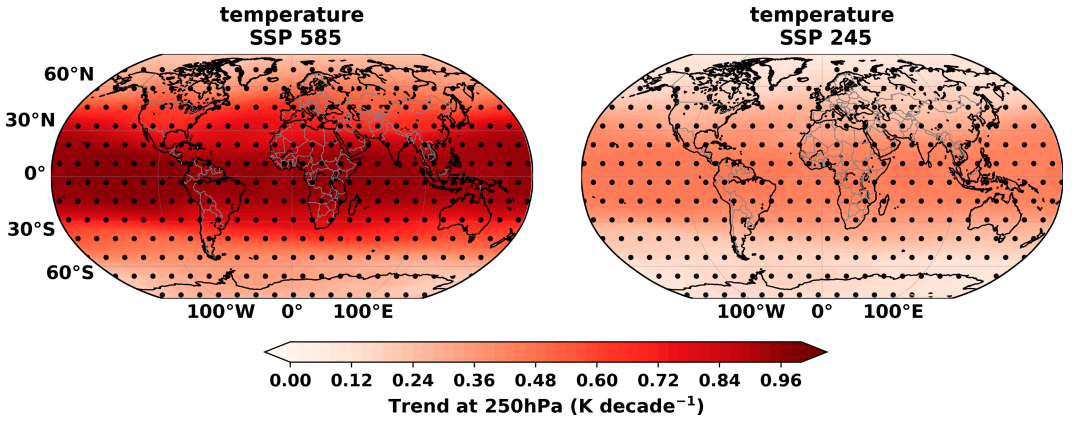

FIG. 2. Multimodel mean of the annual-mean temperature trends at 250 hPa over the period 2015–2100, for SSP 585 and SSP 245. Statistically significant trends (stippled) where the p value is ≤0.05.

the characteristics of the meridional temperature gradient and land–sea contrasts of the Southern Hemisphere (Yeung et al. 2021; O'Kane et al. 2024). Prior studies have shown that Hadley cell expansion and subtropical jet shifts tend to be more pronounced in the Southern Hemisphere (e.g., Lu et al. 2007; Adam et al. 2014) and that stratospheric ozone recovery in the SH can further amplify upper-level wind changes (Polvani et al. 2011). Future climate studies have also shown that westerly winds consistently increase in future projections (Wang 2013). Thus, we observe a continuously increasing mean trend of both annual-mean zonal speed and annual-mean vertical wind shear.

Seasonal analysis (not shown) reveals that during Northern Hemisphere winter, dynamical structures—particularly vertical shear and stratification structure—briefly resemble those in the Southern Hemisphere, suggesting a seasonal weakening of hemispheric asymmetries. However, these asymmetries remain strong in summer, reinforcing the relevance of focusing on annual-mean trends to capture robust, hemispherical distinct signals.

The observed increasing vertical wind shear aligns with findings from Lee et al. (2019) and Lv et al. (2021), who documented enhanced meridional temperature gradients leading to stronger upper-level jets and increased turbulence in the jet stream. These findings emphasize the critical influence of thermal wind balance on atmospheric dynamics (Wallace and Hobbs 2006), particularly as the warming climate alters temperature distributions and jet stream behaviors across both hemispherical midlatitudes.

Focusing on the tropical latitudes of Fig. 1, both the tropical Northern Hemisphere and Southern Hemisphere vertical profiles for both SSPs show a mix of weakening and small positive mean trends of the annual-mean vertical wind shear in the lower–midtroposphere, accompanied by an increase in the upper troposphere.

In the tropics (0°–30°N and 0°–30°S), warming under increased greenhouse gas concentrations leads to a characteristic vertical structure of atmospheric temperature change. As surface temperatures rise, the moist adiabatic lapse rate decreases, resulting in amplified warming in the mid- to upper troposphere (Held and Soden 2000; Santer et al. 2005; Vecchi and Soden 2007). This response is a robust feature of climate model projections and reflects thermodynamic adjustments rather than internal modes of variability (Held and Soden 2006). Consequently, vertical wind shear and temperature gradients in these layers are modified primarily through changes in atmospheric stability associated with a warmer and moister troposphere (Held and Soden 2006; Shaw and Miyawaki 2024).

b. *Thermal wind balance*

As mentioned in the previous sections, the observed vertical shear trends in both hemispherical latitudinal regions, particularly the increasing trend at upper levels, are closely tied to changes in temperature and can be interpreted through the thermal wind balance. For this analysis, we applied the formulation that relates the vertical shear of the gradient zonal wind to the meridional temperature gradient, incorporating both Coriolis and centrifugal effects. The balance, as shown by Knox (1997), can be expressed in the following two equivalent forms:

$$\frac{\partial}{\partial p}\left(\frac{u_{\mathrm{gr}}^2}{fR}+u_{\mathrm{gr}}\right)=\frac{R_d}{fp}\frac{\partial T}{\partial y},$$

$$\frac{\partial u_{\mathrm{gr}}}{\partial p}=\left(\frac{R_d}{fp}\frac{\partial T}{\partial y}+\frac{u_{\mathrm{gr}}^2}{fR^2}\frac{\partial R}{\partial p}\right)\left(1+\frac{2u_{\mathrm{gr}}}{R}\right), \tag{3}$$

where $\partial u_{\mathrm{gr}}/\partial p$ represents the vertical shear of the gradient zonal wind and $\partial T/\partial y$ corresponds to the meridional temperature gradient. The R_d is the specific gas constant for dry air, f is the Coriolis parameter, R is the curvature radius, p is the pressure, T is the mean temperature field (in this instance, the averaged layer between 200 and 300 hPa), u_{gr} is the mean gradient zonal wind speed, and y is the northward distance.

We start by presenting the ensemble trends of the global annual-mean temperature field at 250 hPa for both SSPs (Fig. 2).

Both hemispheres exhibit a distinct mean trend of the annual-mean temperature field at 250 hPa, characterized by warmer conditions (stronger trends) near the equator and progressively cooler temperatures (weaker trends) toward the poles, with trends statistically significant in all models and the

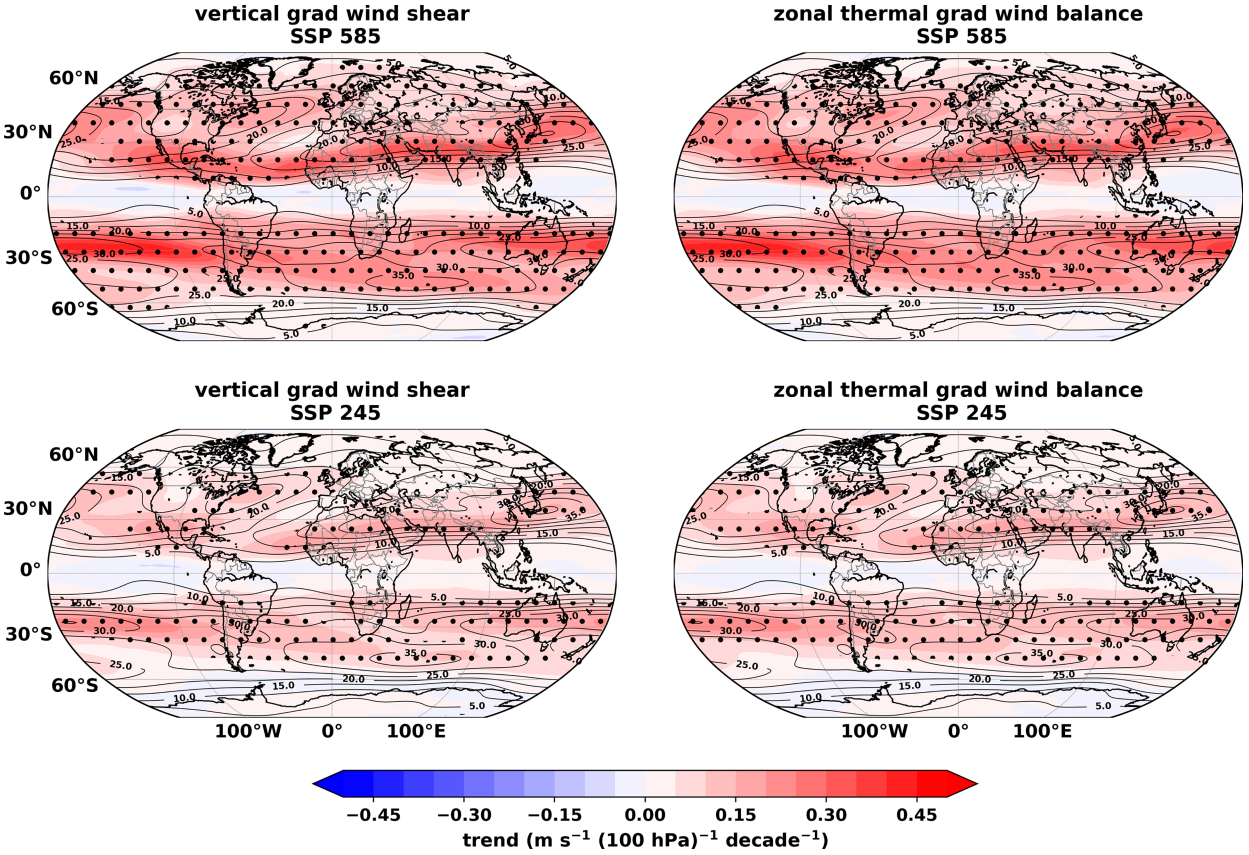

FIG. 3. Multimodel ensemble mean of the annual-mean trends in vertical shear of gradient zonal wind at 250 hPa [left side of Eq. (3) is presented on the left and the right side on the right] for both (top) SSP 585 and (bottom) SSP 245. Statistically significant trends (stippled) where the p value was ≤0.05. The black contours represent the 2015–2100 annual-mean zonal wind at 250 hPa, plotted at 5 m s^{-1} intervals.

multimodel ensemble. Figure 2 is therefore depicting a clear meridional gradient of the annual-mean trend in both SSPs (585 is always more intense in magnitude than 245).

We will now analyze the relationship between the meridional temperature gradient and the vertical shear of the gradient zonal wind. For this purpose, we have computed both sides of the thermal wind balance equation [Eq. (3)].

Figure 3 displays the multimodel mean trends in vertical annual-mean wind shear computed from both sides of the thermal wind balance equation [Eq. (3)] at 250 hPa for the high-emission scenario (SSP 585; top row) and the intermediate scenario (SSP 245; bottom row). The left panels represent the mean trends of vertical shear of the zonal gradient wind derived by the centered differences in Eq. (1), while the right panels show the vertical shear mean trends reconstructed from the meridional temperature gradient and the vertical gradient of the centrifugal term, in accordance with the thermal wind balance applied to gradient wind.

Both emission scenarios exhibit an overall increase in vertical wind shear, especially in the subtropical regions of both hemispheres. The most pronounced trends occur under the SSP 585 scenario, particularly near 30°N and 30°S. This is consistent with previous studies that project a strengthening and poleward shift of the upper-level jet streams in response to increased greenhouse gas forcing (Yin 2005; Lorenz and DeWeaver 2007; Barnes and Polvani 2013). These shifts are associated with intensified meridional temperature gradients in the upper troposphere, which, in turn, enhance vertical wind shear near the subtropical jets (Gettelman et al. 2011). For example, Lu et al. (2007) showed that global warming intensifies the temperature gradient near the tropopause, strengthening vertical wind shear in subtropical regions. Similarly, Aiyyer and Thorncroft (2006) emphasized the sensitivity of tropical vertical shear patterns to large-scale atmospheric changes. The agreement between the two sides of the thermal wind equation supports the use of this balance to interpret large-scale dynamical responses in future climate projections (Trenberth and Stepaniak 2003; Butler et al. 2010; Shepherd 2014).

To quantify how both sides relate to each other and how significant this relation is, we computed both coefficients of correlation for both SSPs (see Fig. 4). For each grid point, Pearson's correlation coefficient was calculated over the 86-yr period to assess the relationship between the annual-mean vertical wind shear derived from the left side of Eq. (3) and that from the right side of Eq. (3), with statistically significant correlations highlighted (stippled) where the p value was

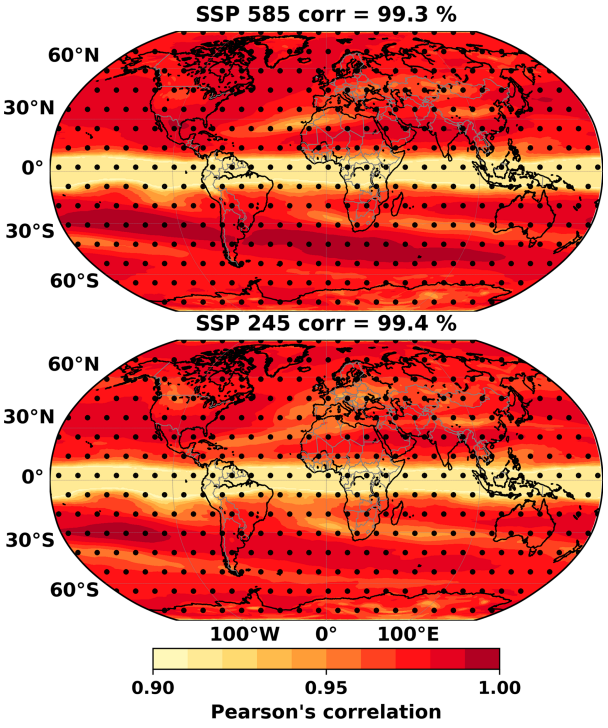

FIG. 4. Pearson's correlation coefficient for the annual means of the multimodel ensemble mean between vertical shear computed as the centered difference in zonal-mean gradient wind speeds for 250 hPa and the vertical shear computed by the meridional temperature gradient and the centrifugal term on the right side of Eq. (3). The coefficients computed with a significance $> 95\%$ (p value < 0.05) were stippled, and the area-weighted pattern correlation coefficient was annotated in the subtitle.

<0.05. Additionally, an area-weighted pattern correlation coefficient was computed to quantify the agreement between the annual-mean trends in vertical shear from both sides of Eq. (3) across the entire time series and the globe.

The results presented in Fig. 4 display an overall significant agreement between both sides of the thermal balance equation for the vertical mean gradient wind shear, with an overall global spatial coefficient correlation of 99.3% for SSP 585 and 99.4% for SSP 245, thus giving a statistical significance for the increasing trends in the annual-mean vertical shear across the globe.

Despite this overall agreement, certain regions—such as the eastern North Atlantic and the Tibetan Plateau—exhibit weaker (albeit still above 90%) correlation between vertical shear and meridional temperature gradient trends. In these areas, local dynamical and topographic influences likely disrupt the thermal wind balance: Over the Plateau, elevated terrain and weakened westerlies undermine the shear–temperature relationship (Wu et al. 2012; Li et al. 2020; Fan et al. 2022; Zeng et al. 2024; Ge et al. 2017), while in the Atlantic, variability in the jet stream, baroclinicity, and ocean-driven heat transport introduce additional complexity (Simmons 2022).

Moreover, the spatial distributions of the trends in Fig. 3 also seem to agree with studies published by Lee et al. (2019) and Lv et al. (2021) where increasing trends of vertical mean wind shear were observed in the regions of the North Atlantic more prominent around 40°–50°N and in the Eurasian around 30°–40°N, while Bell et al. (2019) observed an increase in the vertical mean wind shear around 30°–40°S (subtropical jet) when studying the projections for tropical cyclone track density in the Southern Hemisphere.

c. *Meridional temperature gradient*

We turn our attention now to assessing the vertical structure of the meridional temperature gradient. For this purpose, we computed the differences in the annual-mean temperature at each pressure level between two weighted averaged regional boxes over the Northern Hemisphere (Southern Hemisphere) mid- and tropical latitude regions, namely, a subtropical box [30°–50°N/S, from 180°W to 180°E] and a polar box [50°–70°N/S, from 180°W to 180°E] for the midlatitudes and a lower tropical box [0°–15°N/S, from 180°W to 180°E] and upper tropical box [15°–30°N/S, from 180°W to 180°E] for the tropical latitudes, yielding a zonal-mean bulk meridional temperature difference. The mean trends for this quantity are presented in Fig. 5 for the four regions.

The Northern Hemisphere midlatitude trends show a clear distinction between a lower and upper troposphere, where SSP 585 depicts the weakening of the meridional gradient in the lower troposphere associated with Arctic amplification (Stuecker et al. 2018) and a strengthening in the levels above, likely associated with the tropical warming, which will increase the temperature gradient at those levels (Barnes and Screen 2015; Francis et al. 2017). The SSP 245 shows a similar distribution but at a lower intensity. We see an ensemble decrease down to -0.25 K decade^{-1} in the SSP 585 and -0.15 K decade^{-1} in SSP 245 for the lower troposphere and an increase up to 0.4 K decade^{-1} for SSP 585 and 0.2 K decade^{-1} for SSP 245 in the upper troposphere. This clearly depicts how the climate is adapting to the anthropogenic emission scenarios (Haarsma et al. 2013), with a greater response to emission increase.

The Southern Hemisphere midlatitudes (Fig. 5) depict a slightly different profile: There is no/little lower-level weakening. Compared to the strong polar amplification in the Northern Hemisphere, the Southern Hemisphere polar amplification is much weaker (Caporale et al. 2024). Salzmann (2017) attributed part of this asymmetry to the contrasting elevations of Antarctica and the Arctic, with simulations suggesting that lower Antarctic topography would result in stronger warming responses. However, given that the 50°–70°S latitude band considered here primarily encompasses the Southern Ocean rather than the Antarctic continent itself, oceanic processes are likely more influential in this region. In particular, the Southern Ocean is known to exhibit delayed and weakened warming due to strong upwelling of cold deep waters, deep mixed layers, and efficient ocean heat uptake, which act as a buffer against surface warming (Armour et al. 2016; Marshall et al. 2014; Swart et al. 2018). Despite this muted surface response, a modest strengthening of the meridional temperature gradient is still evident in the upper troposphere, with warming rates between

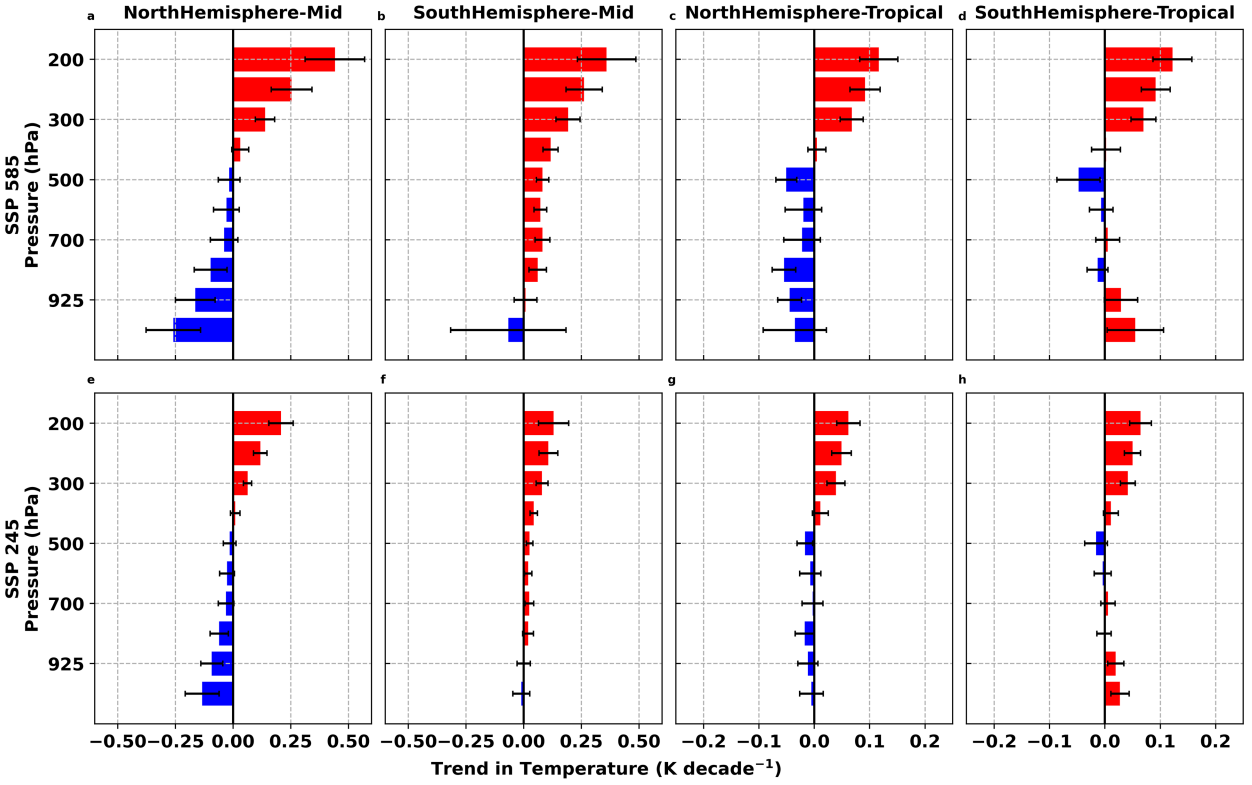

FIG. 5. Vertical profiles of trends in the annual-mean north–south temperature difference across the NH-M/SH-M and NH-T/SH-T over the period 2015–2100. (top) SSP 585 and (bottom) SSP 245. Error bars indicate the intermodel standard deviation, representing model spread.

0.2 and 0.4 K decade^{-1} at 250–200 hPa under SSP 585 and up to 0.15 K decade^{-1} under SSP 245.

Figure 5 therefore depicts the meridional temperature differences between subtropical and polar regions, highlighting Arctic-driven amplification in the Northern Hemisphere midlatitudes, which weakens temperature gradients (Stuecker et al. 2018) and reduces wind shear at lower altitudes up to 500 hPa. In addition to Arctic amplification, models seem to be consistent in projecting amplified warming in the tropical upper troposphere (Barnes and Screen 2015; Francis et al. 2017). Unlike polar amplification, which reduces the poleward temperature gradient, this feature will increase the equator-to-pole gradient at these upper-tropospheric levels. In contrast, the Southern Hemisphere midlatitudes, with fewer landmasses, lower surface albedo feedback, and higher ocean heat uptake, exhibit less extreme thermal gradients but positive temperature trends at most levels, with some weak negative trends near the surface. These trends correspond to consistent zonal wind speed increases (Smith et al. 2019; Zhu et al. 2023; Yeung et al. 2021; O'Kane et al. 2024). This differential hemispheric heating underscores the impact of polar amplification (stronger in the Northern Hemisphere midlatitudes; Caporale et al. 2024) and atmospheric dynamics on projected vertical wind shear across latitudes under future climate scenarios (Casagrande et al. 2020; Ren and Lynch 2024).

d. Vertical wind shear: Upper troposphere

To evaluate the effects of an intensified meridional temperature gradient at 250 hPa on atmospheric circulation, Fig. 6 shows the multimodel ensemble mean and spread of the annual-mean vertical wind shear at 250 hPa, along with zonal-mean wind speeds at 200 and 300 hPa across midlatitudes in both hemispheres, based on data from the 26 models. Wind shear at 250 hPa was calculated using the centered difference between 200 and 300 hPa, allowing for an optimal level to observe trends in vertical wind gradients.

The results visibly indicate an increase in 250-hPa wind shear over time, driven by contrasting trends in zonal wind speeds at 200 and 300 hPa. Specifically in the Northern Hemisphere midlatitudes, a sharp rise at 200 hPa alongside a decline at 300 hPa creates a growing differential, intensifying wind shear at 250 hPa. As shown in Fig. 6, multimodel ensemble means reveal statistically significant increases in vertical wind shear and zonal wind speeds, with values for vertical wind shear in the range of 16%–34% [or 0.04–0.08 m s^{-1} (100 hPa)$^{-1}$ decade^{-1}] for both SSP scenarios over the Northern Hemisphere midlatitudes for the 86-yr period and across the 26 models (Table 2). This aligns with the findings of Simpson (2016), who observed an increase in westerly winds at 200 hPa in response to rising greenhouse gas concentrations.

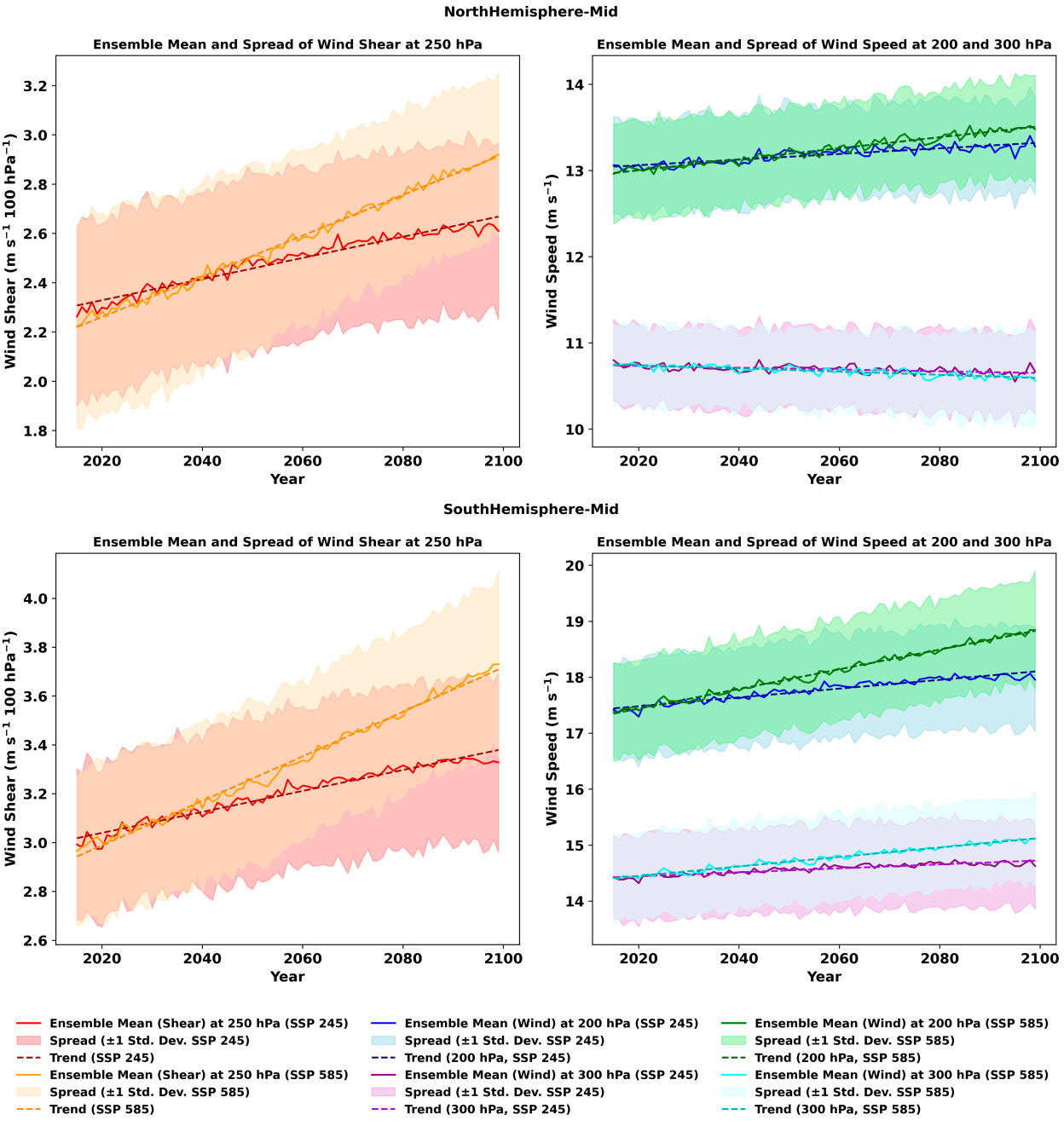

FIG. 6. Multimodel ensemble mean and spread across the 26 models for (left) vertical wind shear at 250 hPa and (right) wind speeds at 200 and 300 hPa over the period 2015–2100 for the (top) NH-M and (bottom) SH-M and both SSPs.

Projected trends in mean zonal wind speeds at 200- and 300-hPa levels show notable hemispheric contrasts under SSP scenarios (Fig. 6 and Table A1 in the appendix section). In the Northern Hemisphere midlatitudes, positive trends are observed at 200 hPa with negative trends at 300 hPa, while the Southern Hemisphere midlatitudes display positive trends at both levels. This asymmetry likely arises from vertical temperature profile and meridional temperature gradient differences (see Fig. 5), influenced by polar amplification, tropical warming, and land–sea contrasts (Archer and Caldeira 2008; Nakamura et al. 2004; Lee 2014; Abish et al. 2015).

e. Stability and Ri

Given the clear link between meridional temperature gradients, vertical wind shear, and zonal wind speed trends discussed above, it is essential to further explore the role of atmospheric stability in shaping these dynamics. Atmospheric stability influences how vertical wind gradients evolve, particularly in regions

TABLE 2. Annual-mean trend metrics over the NH-/SH-M and NH-/SH-T: vertical wind shear, N^2, and Ri at 250 hPa. The percentage change is the total relative increase/decrease over the 86-yr period.

SSP	Region	Shear trend [m s^{-1} (100 hPa)$^{-1}$ $decade^{-1}$]	Shear change (%)	N^2 trend (10^{-4} s^{-2} $decade^{-1}$)	N^2 change (%)	Ri trend ($decade^{-1}$)	Ri change (%)
585	NH-M	0.083	34.65	−0.040	−20.51	−0.050	−47.06
585	SH-M	0.091	26.08	−0.038	−19.49	−0.030	−69.87
585	NH-T	0.108	28.97	0.014	12.99	−0.003	−2.49
585	SH-T	0.112	27.02	0.012	11.00	−0.004	−3.95
245	NH-M	0.043	16.09	−0.021	−11.08	−0.025	−20.62
245	SH-M	0.043	11.21	−0.018	−10.05	−0.014	−38.16
245	NH-T	0.059	20.65	0.005	4.50	−0.003	−4.50
245	SH-T	0.060	17.00	0.004	3.56	−0.003	−1.59

with intensified meridional temperature contrasts (Holton 2004; Held and Hou 1980). To quantify this, we computed the yearly means of the Brunt–Väisälä frequency squared N^2 [Eq. (4)], a metric that measures the resistance of air parcels to vertical displacement. By examining N^2 trends, we gain insight into how changes in thermal stratification contribute to the observed variations in vertical wind shear and the broader atmospheric circulation patterns:

$$N^2 = \frac{g}{\theta}\frac{\partial\theta}{\partial z}, \tag{4}$$

where g is the acceleration due to gravity, θ is the potential temperature, z is the height, and the vertical displacement ∂z is given by

$$\partial z = -\frac{R_d T}{pg}\partial p. \tag{5}$$

The change in mean annual stability along with vertical wind shear is crucial for understanding turbulence dynamics, as it influences the Richardson number Ri and the ratio of buoyant forces to shear forces (N^2/shear^2). When the Ri number is low (less than 1/4), the atmosphere becomes unstable, favoring the development of turbulence, including CAT (Sharman and Pearson 2017).

To compute Ri, vertical wind shear had to be computed in its standard Système International (SI) units of per second (s^{-1}) in contrast with what has been presented so far [m s^{-1} (100 hPa)$^{-1}$]. The ratio N^2/shear^2 (s^{-2}/s^{-2}) was then computed for the global grid from the monthly means, and then, the yearly and regional means were computed for Ri. For continuity and easy comparison with the previous sections, the following figures will still show annual-mean vertical wind shear [m s^{-1} (100 hPa)$^{-1}$].

Figure 7 presents a side-by-side visual analysis of the mean latitudinal yearly mean trends in vertical shear of zonal wind, Brunt–Väisälä frequency squared N^2, Richardson number, and air temperature at 250 hPa. These variables are shown together because they are physically interconnected: Temperature influences vertical wind shear and N^2, and the ratio between these will, in turn, affect the Richardson number.

Results show a robust latitudinal pattern: positive trends in the tropics for N^2 (30°S–30°N) and negative trends in the extratropics, with peak negative trends around 50°–60° in both hemispheres. The positive tropical trends are consistent with tropical amplification, where upper-tropospheric warming exceeds surface warming due to the decreasing moist adiabatic lapse rate in a warmer climate (Held and Soden 2006; Shepherd 2014). In contrast, midlatitude and polar regions exhibit greater near-surface warming, reducing the vertical gradient of potential temperature and hence decreasing N^2 (Lu et al. 2007; Singh and O'Gorman 2012). Moreover, the peak negative trends at 50°–60° correspond to regions near the poleward flanks of the jet streams and the transition zone between tropical and extratropical tropopause regimes. Climate change is known to induce poleward shifts of the midlatitude jets and weakening of the Hadley circulation (Yin 2005), as well as tropopause elevation and stratospheric cooling, all contributing to reduced static stability near 250 hPa in these latitudes (Shaw et al. 2016; Shepherd 2008; Singh and O'Gorman 2012).

The observed decreasing trends in N^2 and increasing trends in vertical shear of zonal wind are consistent with the overall decline in the Richardson number annual-mean trends. As outlined earlier in this section, the annual trend in Ri is derived from the yearly means of monthly N^2/shear^2 values rather than from the ratio of the respective annual trends of N^2 and shear^2. Notably, Ri trends follow those of N^2 more closely, but positive Ri trends are confined to a narrow equatorial band between approximately 5°S and 5°N, largely because vertical wind shear trends peak in the subtropics, thereby limiting positive Ri trends outside this region.

Research by Sharman et al. (2014) suggests that when Ri is low, the potential for CAT increases, especially in regions of high wind shear such as the subtropical jet and subpolar jet. The heightened potential for CAT events in a warming climate (Smith et al. 2023) is further exacerbated by changes in atmospheric dynamics, including shifts in the jet stream and the weakening of the Hadley circulation (Yin 2005; Lionello et al. 2024), which influence both wind shear and atmospheric stability.

Figure 8 shows the annual-mean trends of vertical shear of zonal wind, N^2, and Ri for the Northern and Southern Hemisphere midlatitude regional boxes at 250 hPa.

Figure 8 and Table 2 indicate a clear tendency for an increase in the annual-mean vertical wind shear and a decrease in the annual-mean stability in both hemispherical regions. As the annual-mean vertical wind shear increases and the mean

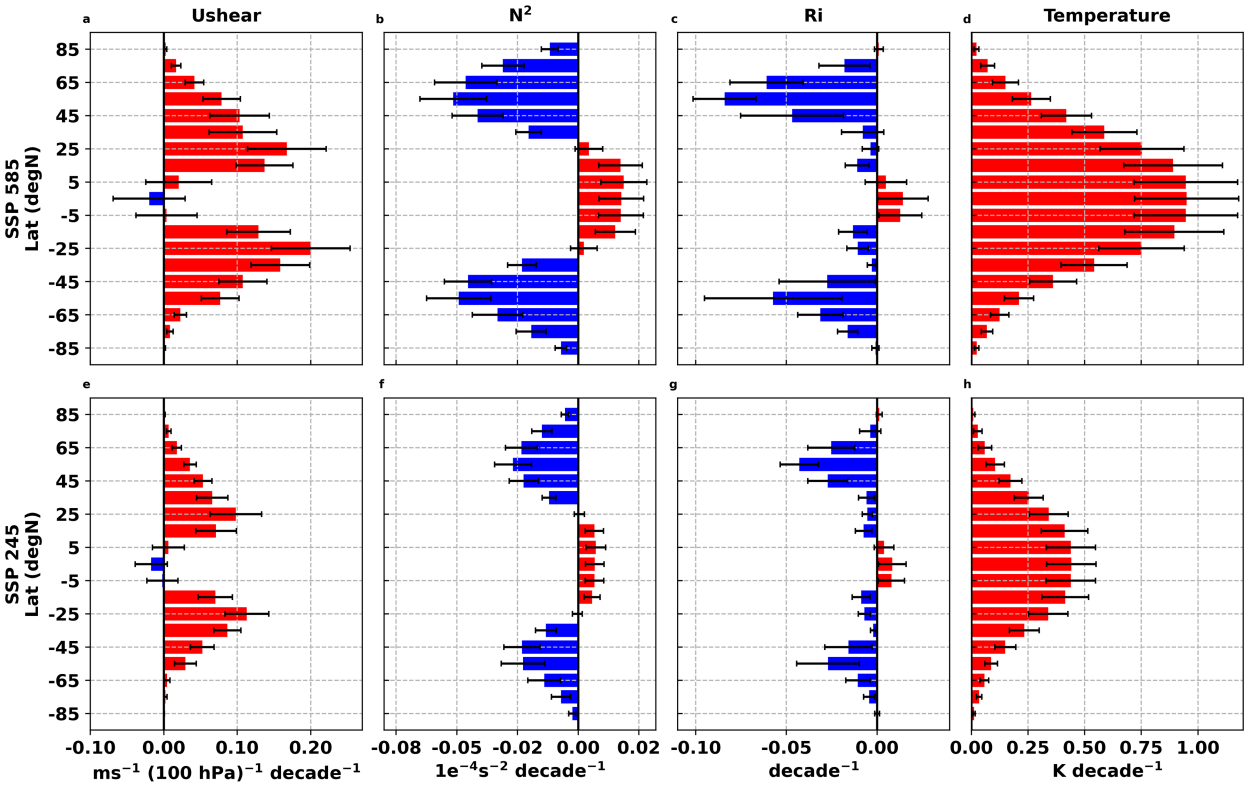

FIG. 7. Zonal-mean trends of annual-mean vertical wind shear, annual-mean N^2, annual-mean Ri, and annual-mean temperature, across latitudinal bands for both SSPs (top) 585 and (bottom) 245 at 250 hPa from 2015 to 2100. Weighted averages are taken over each 10° latitudinal band. Error bars indicate the intermodel standard deviation, representing model spread.

stability decreases, it is expected that the Ri will respond accordingly, which can in return increase the frequency of CAT events in the changing climate. In fact, Fig. 8 shows a decreasing trend of Ri over all regions and scenarios, with the worst scenario (SSP 585) exhibiting stronger trends. These findings agree with the study by Lee et al. (2023) who found regional patterns of lowered Ri (over a 44-yr reanalysis period) being consistent with the patterns of N^2 and vertical wind shear indicating low static stability induced by storm tracks and large shear instability at the exit region of the jet, respectively. Table 2 provides a more detailed overview of the trend metrics for both hemispheric regional boxes and SSP scenarios. All the values are statistically significant with p values < 0.01. Positive values denote an increase, and negative values denote a decrease.

To complement the analysis of mean trends, Table 3 highlights the 99th-percentile behavior of vertical wind shear, static stability N^2, and Richardson number Ri. In the midlatitudes, the 99th-percentile shear ensemble increases substantially (e.g., 24.80% in NH-M under SSP 585), with modest corresponding ensemble decreases in N^2, resulting in sharp declines in extreme Ri values—down to −58% in SH-M. This indicates a growing prevalence of dynamically unstable conditions in the upper tail, which are particularly relevant for aviation hazards like CAT (Sharman et al. 2006).

However, in the tropics, while high-end ensemble shear also increases (e.g., 25.03% in NH-T), N^2 trends are positive, which tempers the Ri response, resulting in much smaller reductions in extreme Ri values (from −3.3% to −4.7%). This further reinforces that in tropical regions, increasing shear alone does not drive stronger instability due to compensating increases in static stability. These regional contrasts highlight that the impact of climate change on upper-tropospheric instability is not spatially uniform and emphasize the need to consider regional dynamics when assessing the implications for turbulence and jet-related instabilities. While the midlatitude changes—marked by increased vertical shear and reduced static stability—are consistent with conditions that favor clear-air turbulence (Sharman et al. 2014), the tropics present a different picture. Here, despite increased shear, the rise in stability may mitigate the development of CAT-like conditions. However, the evolving background environment could still foster other types of turbulence, such as convectively induced turbulence (CIT) and NCT, especially given the prevalence of deep convection in these regions. Recent work (e.g., Kim et al. 2023) underscores the potential for increased CIT and NCT under warming scenarios. We therefore acknowledge that while our diagnostics are not specific to convective turbulence, the observed changes may still reflect broader shifts in turbulence-prone conditions, particularly in the tropics. Future work employing convection-resolving models could further clarify these dynamics.

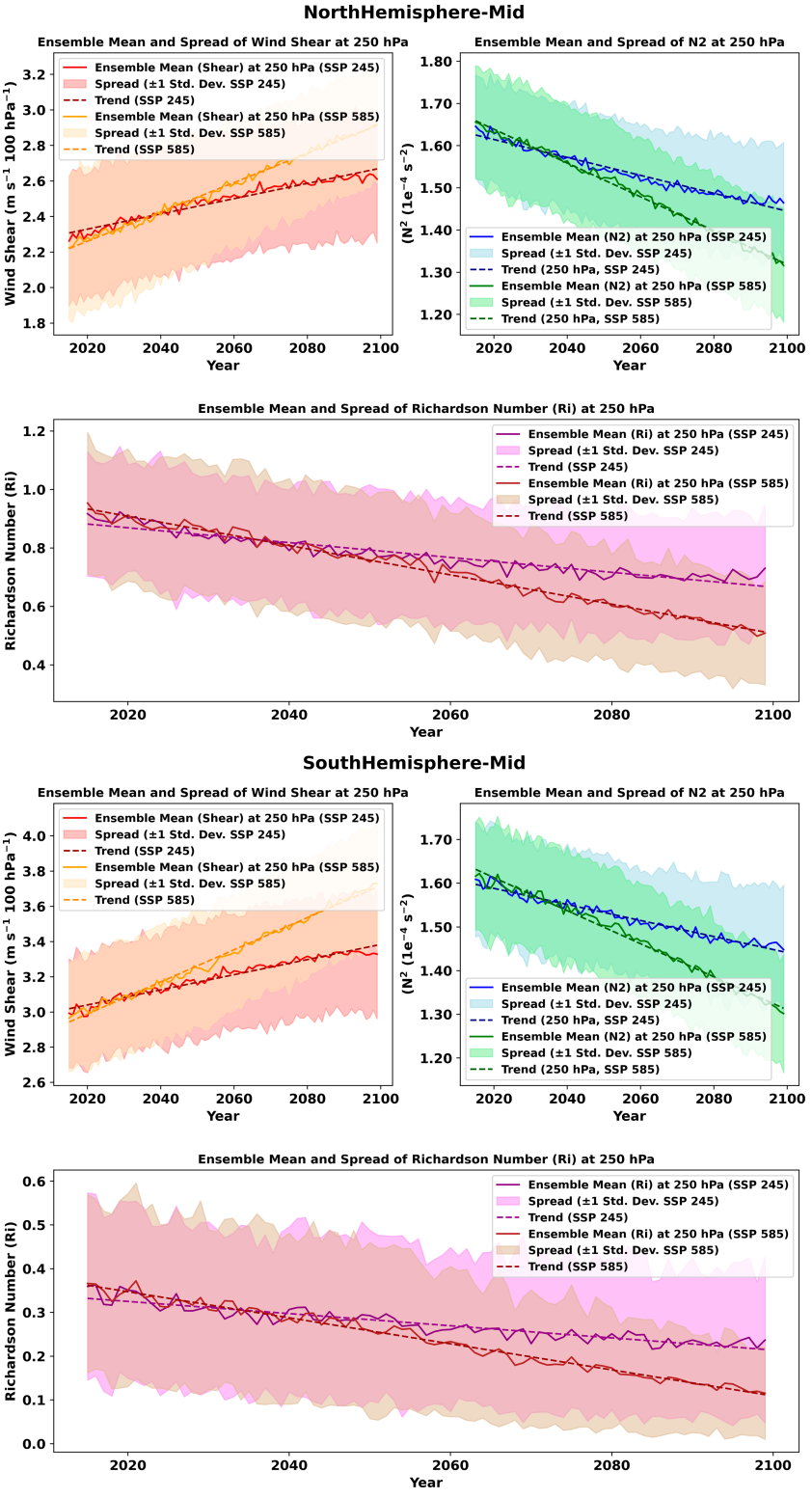

FIG. 8. Multimodel ensemble mean and spread across the 26 models for the annual means of (left) wind shear at 250 hPa, (right) N^2 at 250 hPa, and (bottom) Ri at 250 hPa over the period 2015–2100 and both SSPs for the regional boxes over the NH-M and SH-M, respectively.

TABLE 3. 99th-percentile metrics over the NH-/SH-M and NH/SH–T: vertical wind shear at 250 hPa, N^2 at 250 hPa, and Ri at 250 hPa. The percentage change is the total relative increase/decrease.

Region	SSP	Shear p99 change (%)	N^2 p99 change (%)	Ri p99 change (%)
NH-M	585	24.80	−13.02	−41.98
SH-M	585	19.56	−12.32	−58.23
NH-T	585	25.03	11.52	−4.71
SH-T	585	21.75	9.92	−3.33
NH-M	245	11.94	−8.09	−22.41
SH-M	245	8.52	−7.15	−27.75
NH-T	245	14.72	3.82	−4.27
SH-T	245	12.53	3.30	−3.92

4. Summary and discussion

Climate change appears to have a significant impact on trends in the annual-mean vertical wind shear, particularly around the core of the upper-level jet streams at 250 hPa (Shaw and Miyawaki 2024; Lee et al. 2019). The projected temperature increase in values between 0.25 and 0.4 K decade^{-1} at midlatitudes and 0.6–0.9 K decade^{-1} between tropics under SSP 585 across models shows a clear effect on the meridional temperature gradient at 250 hPa and moreover on the associated vertical wind shear and wind thermal balance. The multimodel ensemble annual mean for vertical wind shear shows an increase per decade between 0.08 and 0.12 m s^{-1} (100 hPa)$^{-1}$ under SSP 585 and 0.04–0.06 m s^{-1} (100 hPa)$^{-1}$ under SSP 245 across several latitudes and both hemispheres. This increasing trend in the annual-mean vertical shear is accompanied by a total decrease/increase in N^2, with the multimodel ensemble mean values between 13% over the Northern Hemisphere tropical latitudes and −20% over the Northern Hemisphere midlatitudes under SSP 585 and between 3.5% over the Southern Hemisphere tropical latitudes and −11% over the Northern Hemisphere midlatitudes under SSP 245 over the 86 years analyzed. The relationship between the increase/decrease in vertical wind shear and buoyancy forces N^2 drives a change in the Richardson number, as it adjusts to temperature shifts in a changing climate. We note a decrease in the annual ensemble mean trends for Ri ranging from −69% to −47% over the Southern and Northern Hemisphere midlatitudes, respectively, under SSP 585, and from −38% to −20% over Southern and Northern Hemisphere midlatitudes, respectively, under SSP 245, for the 2015–2100 period. This suggests that climate change may lead to an increased frequency and intensity of clear-air turbulence (CAT), especially in regions influenced by the upper-level jet streams, as the evolving vertical wind shear and reduced buoyancy forces create more favorable conditions for turbulence generation (Sharman et al. 2014; Lee et al. 2023). Additionally, Smith et al. (2023) found an increase in CAT events over the North Atlantic using a multimodel approach over the period of 1950–2050, reinforcing the need for further investigation and action regarding air safety in a more turbulent future.

Despite the fact that the relatively coarse resolution of CMIP6 models poses a challenge to our ability to accurately assess long-term turbulence variations, the observed increases in annual-mean vertical wind shear and decreases in the annual-mean stability N^2 and consequently in the Ri remain important results. These changes are indicative of large-scale atmospheric conditions becoming increasingly favorable for turbulence. While these models lack the spatial granularity required to resolve localized turbulence intensity or frequency, the emerging trends carry meaningful implications—such as heightened risks for clear-air turbulence, which can affect aviation safety, and greater turbulent mixing across the tropopause. These models, however, lack the detail needed to fully capture these effects (Shapiro 1980; Stohl et al. 2003, 2004), and the turbulent mixing is crucial as it influences large-scale atmospheric thermodynamics and dynamics (Huang et al. 2013).

It is important to emphasize that large-scale indicators—such as enhanced vertical wind shear and reduced static stability—act as necessary but not sufficient precursors to turbulence. The emergence of actual turbulence, whether CAT or other forms like convectively induced turbulence (CIT) or near-cloud turbulence (NCT), results from complex and nonlinear processes that operate at smaller spatial and temporal scales (Lane et al. 2004; Kim and Chun 2010; Kim et al. 2014; Trier et al. 2022; Lee et al. 2025). These include gravity wave breaking, shear instabilities, and interactions with moist convection—phenomena that lie beyond the resolution of global climate models. As such, while our findings point to an increasing predisposition for turbulence under climate change, they should not be interpreted as evidence of a direct or linear increase in turbulence occurrence or severity.

This distinction underscores the importance of future studies employing high-resolution models or dynamical downscaling techniques to better capture the multiscale pathways connecting large-scale climate signals to aircraft-scale turbulence. As more refined datasets and modeling tools become available, they will enable more detailed assessments of how climate-driven shifts in jet stream structure and stability affect both the prevalence and intensity of upper-tropospheric turbulence.

Acknowledgments. This work has been funded by the SCENARIO NERC Doctoral Training Partnership Grant NE/S007261/1.

Data availability statement. The CMIP6 information and data can be found at https://wcrp-cmip.org/.

APPENDIX

Supplemental Information

Figure A1 shows the multimodel annual-mean trends of vertical wind shear, N^2, and Ri for the Northern Hemisphere 0°–70°N (Southern Hemisphere 0°–70°S) regional boxes, highlighting the increase/decrease ratio between these two quantities.

Table A1 shows with more detail the metrics for annual-mean and 99th-percentile trends for the zonal wind speeds at 300 and 200 hPa for both hemispherical regional boxes in the NH-/SH-M and NH-/SH-T and SSPs across all 26 models. All the values are statistically significant with p values < 0.01, positive values denote an increase, and negative values denote a decrease.

TABLE A1. Annual-mean and 99th-percentile trend metrics for the wind speed variables for the NH-/SH-M and NH-/SH-T boxes. The percentage change is the total relative increase/decrease over the 86-yr period.

SSP	Region	Wind 200-hPa trend (m s^{-1} $decade^{-1}$)	Wind change (%)	p99 change (%)	Wind 300-hPa trend (m s^{-1} $decade^{-1}$)	Wind change (%)	p99 change (%)
585	NH-M	0.06	4.05	3.41	−0.02	−1.64	−0.64
585	SH-M	0.18	8.42	6.89	0.09	4.86	4.26
585	NH-T	0.12	7.22	8.56	0.01	−0.98	2.89
585	SH-T	0.15	9.30	9.80	0.04	2.59	5.26
245	NH-M	0.03	1.69	1.97	−0.01	−1.19	−0.28
245	SH-M	0.08	3.06	2.98	0.04	1.38	1.78
245	NH-T	0.08	8.66	6.48	0.02	4.16	3.33
245	SH-T	0.10	7.08	5.53	0.03	3.44	2.86

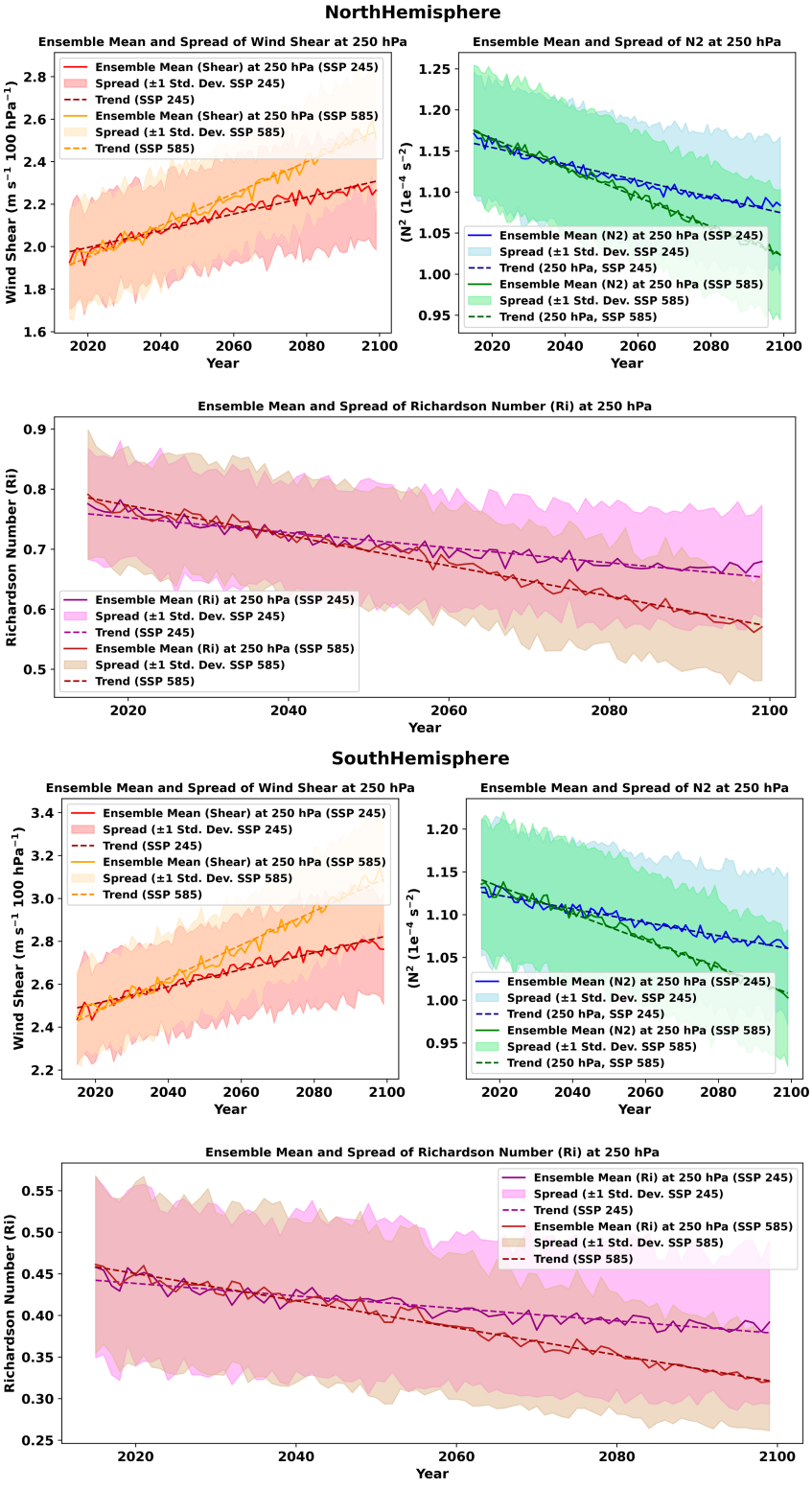

FIG. A1. Multimodel ensemble spread across the 26 models for (left) wind shear, (right) N^2, and (bottom) Ri at 250 hPa over the period 2021–2100 and both SSPs for the regional boxes in the NH (top panels) and SH (bottom panels).

REFERENCES

Abish, B., P. V. Joseph, and O. M. Johannessen, 2015: Climate change in the subtropical jet stream during 1950–2009. *Adv. Atmos. Sci.*, **32**, 140–148, https://doi.org/10.1007/s00376-014-4156-6.

Adam, O., T. Schneider, and N. Harnik, 2014: Role of changes in mean temperatures versus temperature gradients in the recent widening of the Hadley circulation. *J. Climate*, **27**, 7450–7461, https://doi.org/10.1175/JCLI-D-14-00140.1.

Aiyyer, A. R., and C. D. Thorncroft, 2006: Climatology of vertical wind shear over the tropical Atlantic. *J. Climate*, **19**, 2969–2983, https://doi.org/10.1175/JCLI3685.1.

Archer, C. L., and K. Caldeira, 2008: Historical trends in the jet streams. *Geophys. Res. Lett.*, **35**, L08803, https://doi.org/10.1029/2008GL033614.

Armour, K. C., J. Marshall, J. R. Scott, A. Donohoe, and E. R. Newsom, 2016: Southern Ocean warming delayed by circumpolar upwelling and equatorward transport. *Nat. Geosci.*, **9**, 549–554 https://doi.org/10.1038/ngeo2731.

Barnes, E. A., and L. Polvani, 2013: Response of the midlatitude jets, and of their variability, to increased greenhouse gases in the CMIP5 models. *J. Climate*, **26**, 7117–7135, https://doi.org/10.1175/JCLI-D-12-00536.1.

——, and J. A. Screen, 2015: The impact of Arctic warming on the midlatitude jet-stream: Can it? Has it? Will it? *Wiley Interdiscip. Rev.: Climate Change*, **6**, 277–286, https://doi.org/10.1002/wcc.337.

Bell, S. S., S. S. Chand, K. J. Tory, A. J. Dowdy, C. Turville, and H. Ye, 2019: Projections of Southern Hemisphere tropical cyclone track density using CMIP5 models. *Climate Dyn.*, **52**, 6065–6079, https://doi.org/10.1007/s00382-018-4497-4.

Butler, A. H., D. W. J. Thompson, and R. Heikes, 2010: The steady-state atmospheric circulation response to climate change–like thermal forcings in a simple general circulation model. *J. Climate*, **23**, 3474–3496, https://doi.org/10.1175/2010JCLI3228.1.

Caporale, G. M., L. A. Gil-Alana, and N. Carmona-González, 2024: Polar amplification: A fractional integration analysis. CESifo Working Paper 11073, 23 pp., https://doi.org/10.2139/ssrn.4803860.

Casagrande, F., R. Buss de Souza, P. Nobre, and A. Lanfer Marquez, 2020: An inter-hemispheric seasonal comparison of polar amplification using radiative forcing of a quadrupling CO_2 experiment. *Ann. Geophys.*, **38**, 1123–1138, https://doi.org/10.5194/angeo-38-1123-2020.

Colson, D., and H. A. Panofsky, 1965: An index of clear air turbulence. *Quart. J. Roy. Meteor. Soc.*, **91**, 507–513, https://doi.org/10.1002/qj.49709139010.

Dutton, J. A., 1986: *The Ceaseless Wind*. Dover Publications, 617 pp.

Ellrod, G. P., and D. I. Knapp, 1992: An objective clear-air turbulence forecasting technique: Verification and operational use. *Wea. Forecasting*, **7**, 150–165, https://doi.org/10.1175/1520-0434(1992)007<0150:AOCATF>2.0.CO;2.

Endlich, R. M., 1961: Computation and uses of gradient winds. *Mon. Wea. Rev.*, **89**, 187–191, https://doi.org/10.1175/1520-0493(1961)089<0187:CAUOGW>2.0.CO;2.

Fan, W., and Coauthors, 2022: Dominant modes of Tibetan Plateau summer surface sensible heating and associated atmospheric circulation anomalies. *Remote Sens.*, **14**, 956, https://doi.org/10.3390/rs14040956.

Francis, J. A., and S. J. Vavrus, 2015: Evidence for a wavier jet stream in response to rapid Arctic warming. *Environ. Res. Lett.*, **10**, 014005, https://doi.org/10.1088/1748-9326/10/1/014005.

——, ——, and J. Cohen, 2017: Amplified arctic warming and mid-latitude weather: New perspectives on emerging connections. *Wiley Iinterdiscip. Rev.: Climate Change*, **8**, e474, https://doi.org/10.1002/wcc.474.

Ge, F., F. Sielmann, X. Zhu, K. Fraedrich, X. Zhi, T. Peng, and L. Wang, 2017: The link between Tibetan Plateau monsoon and Indian summer precipitation: A linear diagnostic perspective. *Climate Dyn.*, **49**, 4201–4215, https://doi.org/10.1007/s00382-017-3585-1.

Gettelman, A., P. Hoor, L. L. Pan, W. J. Randel, M. I. Hegglin, and T. Birner, 2011: The extratropical upper troposphere and lower stratosphere. *Rev. Geophys.*, **49**, RG3003, https://doi.org/10.1029/2011RG000355.

Gultepe, I., and Coauthors, 2019: A review of high impact weather for aviation meteorology. *Pure Appl. Geophys.*, **176**, 1869–1921, https://doi.org/10.1007/s00024-019-02168-6.

Haarsma, R. J., F. Selten, and G. J. van Oldenborgh, 2013: Anthropogenic changes of the thermal and zonal flow structure over Western Europe and Eastern North Atlantic in CMIP3 and CMIP5 models. *Climate Dyn.*, **41**, 2577–2588 https://doi.org/10.1007/s00382-013-1734-8.

Harvey, B. J., P. Cook, L. C. Shaffrey, and R. Schiemann, 2020: The response of the Northern Hemisphere storm tracks and jet streams to climate change in the CMIP3, CMIP5, and CMIP6 climate models. *J. Geophys. Res. Atmos.*, **125**, e2020JD032701, https://doi.org/10.1029/2020JD032701.

Held, I. M., and A. Y. Hou, 1980: Nonlinear axially symmetric circulations in a nearly inviscid atmosphere. *J. Atmos. Sci.*, **37**, 515–533, https://doi.org/10.1175/1520-0469(1980)037<0515:NASCIA>2.0.CO;2.

——, and B. J. Soden, 2000: Water vapor feedback and global warming. *Annu. Rev. Energy Environ.*, **25**, 441–475, https://doi.org/10.1146/annurev.energy.25.1.441.

——, and ——, 2006: Robust responses of the hydrological cycle to global warming. *J. Climate*, **19**, 5686–5699, https://doi.org/10.1175/JCLI3990.1.

Holton, J. R., 2004: *An Introduction to Dynamic Meteorology*. 4th ed., Elsevier, 535 pp.

Huang, J., E. Bou-Zeid, and J. Golaz, 2013: Turbulence and vertical fluxes in the stable atmospheric boundary layer. Part II: A novel mixing-length model. *J. Atmos. Sci.*, **70**, 1528–1542, https://doi.org/10.1175/JAS-D-12-0168.1.

Jaeger, E. B., and M. Sprenger, 2007: A Northern Hemispheric climatology of indices for clear air turbulence in the tropopause region derived from ERA40 reanalysis data. *J. Geophys. Res.*, **112**, D20106, https://doi.org/10.1029/2006JD008189.

Karnauskas, K. B., J. P. Donnelly, H. C. Barkley, and J. E. Martin, 2015: Coupling between air travel and climate. *Nat. Climate Change*, **5**, 1068–1073, https://doi.org/10.1038/nclimate2715.

Kim, J.-H., and H.-Y. Chun, 2010: A numerical study of clear-air turbulence (CAT) encounters over South Korea on 2 April 2007. *J. Appl. Meteor. Climatol.*, **49**, 2381–2403, https://doi.org/10.1175/2010JAMC2449.1.

——, ——, R. D. Sharman, and S. B. Trier, 2014: The role of vertical shear on aviation turbulence within cirrus bands of a simulated western Pacific cyclone. *Mon. Wea. Rev.*, **142**, 2794–2813, https://doi.org/10.1175/MWR-D-14-00008.1.

——, W. N. Chan, B. Sridhar, R. D. Sharman, P. D. Williams, and M. Strahan, 2016: Impact of the North Atlantic Oscillation on transatlantic flight routes and clear-air turbulence. *J.*

Appl. Meteor. Climatol., **55**, 763–771, https://doi.org/10.1175/JAMC-D-15-0261.1.

Kim, S.-H., J.-H. Kim, H.-Y. Chun, and R. D. Sharman, 2023: Global response of upper-level aviation turbulence from various sources to climate change. *npj Climate Atmos. Sci.*, **6**, 92, https://doi.org/10.1038/s41612-023-00421-3.

Knox, J. A., 1997: Possible mechanisms of clear-air turbulence in strongly anticyclonic flows. *Mon. Wea. Rev.*, **125**, 1251–1259, https://doi.org/10.1175/1520-0493(1997)125<1251:PMOCAT>2.0.CO;2.

Lane, T. P., J. D. Doyle, R. Plougonven, M. A. Shapiro, and R. D. Sharman, 2004: Observations and numerical simulations of inertia–gravity waves and shearing instabilities in the vicinity of a jet stream. *J. Atmos. Sci.*, **61**, 2692–2706, https://doi.org/10.1175/JAS3305.1.

Lee, J. H., J.-H. Kim, R. D. Sharman, J. Kim, and S.-W. Son, 2023: Climatology of clear-air turbulence in upper troposphere and lower stratosphere in the Northern Hemisphere using ERA5 reanalysis data. *J. Geophys. Res. Atmos.*, **128**, e2022JD037679, https://doi.org/10.1029/2022JD037679.

——, ——, S. B. Trier, R. D. Sharman, and J. D. Doyle, 2025: Generation mechanisms of near-cloud turbulence events in the upper-level outflow of tropical cyclone Hagibis. *Mon. Wea. Rev.*, **153**, 521–542, https://doi.org/10.1175/MWR-D-24-0116.1.

Lee, S., 2014: A theory for polar amplification from a general circulation perspective. *Asia-Pac. J. Atmos. Sci.*, **50**, 31–43, https://doi.org/10.1007/s13143-014-0024-7.

Lee, S. H., Williams, P. D. Frame, and T. H. A., 2019: Increased shear in the North Atlantic upper-level jet stream over the past four decades. *Nature*, **572**, 639–642 https://doi.org/10.1038/s41586-019-1465-z.

Li, R., X. Xu, Y. Wang, M. A. C. Teixeira, J. Tang, and Y. Lu, 2020: The response of parameterized orographic gravity waves to rapid warming over the Tibetan Plateau. *Atmosphere*, **11**, 1016, https://doi.org/10.3390/atmos11091016.

Lionello, P., R. D'Agostino, D. Ferreira, H. Nguyen, and M. S. Singh, 2024: The Hadley circulation in a changing climate. *Ann. N. Y. Acad. Sci.*, **1534**, 69–93, https://doi.org/10.1111/nyas.15114.

Lorenz, D. J., and E. T. DeWeaver, 2007: Tropopause height and zonal wind response to global warming in the IPCC scenario integrations. *J. Geophys. Res.*, **112**, D10119, https://doi.org/10.1029/2006JD008087.

Lu, J., G. A. Vecchi, and T. Reichler, 2007: Expansion of the Hadley cell under global warming. *Geophys. Res. Lett.*, **34**, L06805, https://doi.org/10.1029/2006GL028443.

Lv, Y., J. Guo, J. Li, Y. Han, H. Xu, X. Guo, L. Cao, and W. Gao, 2021: Increased turbulence in the Eurasian upper-level jet stream in winter: Past and future. *Earth Space Sci.*, **8**, e2020EA001556, https://doi.org/10.1029/2020EA001556.

Marshall, J., K. C. Armour, J. R. Scott, Y. Kostov, U. Hausmann, D. Ferreira, T. G. Shepherd, and C. M. Bitz, 2014: The ocean's role in polar climate change: Asymmetric Arctic and Antarctic responses to greenhouse gas and ozone forcing. *Philos. Trans. Roy. Soc.*, **A372**, 20130040, https://doi.org/10.1098/rsta.2013.0040.

Nakamura, H., T. Sampe, Y. Tanimoto, and A. Shimpo, 2004: Observed associations among storm tracks, jet streams and midlatitude oceanic fronts. *Earth's Climate: The Ocean-Atmosphere Interaction*, Geophysics Monograph Series, Vol. 147, Amer. Geophys. Union, 329–345.

Newton, C. W., and E. Palmén, 1963: Kinematic and thermal properties of a large-amplitude wave in the westerlies. *Tellus*, **15A**, 99–119, https://doi.org/10.3402/tellusa.v15i2.8836.

O'Kane, T. J., J. S. Frederiksen, C. S. Frederiksen, and I. Horenko, 2024: Beyond the first tipping points of Southern Hemisphere climate. *Climate*, **12**, 81, https://doi.org/10.3390/cli12060081.

O'Neill, B. C., and Coauthors, 2016: The Scenario Model Intercomparison Project (ScenarioMIP) for CMIP6. *Geosci. Model Dev.*, **9**, 3461–3482, https://doi.org/10.5194/gmd-9-3461-2016.

Palmén, E., 1948: On the distribution of temperature and wind in the upper westerlies. *J. Meteor.*, **5**, 20–27.

Pedlosky, J., 1987: *Geophysical Fluid Dynamics.* Springer Verlag, 710 pp., https://doi.org/10.1007/978-1-4612-4650-3.

Polvani, L. M., D. W. Waugh, G. J. P. Correa, and S. Son, 2011: Stratospheric ozone depletion: The main driver of twentieth-century atmospheric circulation changes in the Southern Hemisphere. *J. Climate*, **24**, 795–812, https://doi.org/10.1175/2010JCLI3772.1.

Prosser, M. C., P. D. Williams, G. J. Marlton, and R. G. Harrison, 2023: Evidence for large increases in clear-air turbulence over the past four decades. *Geophys. Res. Lett.*, **50**, e2023GL103814, https://doi.org/10.1029/2023GL103814.

Reed, R. J., and K. R. Hardy, 1972: A case study of persistent, intense, cleat air turbulence in an upper level frontal zone. *J. Appl. Meteor.*, **11**, 541–549, https://doi.org/10.1175/1520-0450(1972)011<0541:ACSOPI>2.0.CO;2.

Ren, D., and M. J. Lynch, 2024: Changes in global aviation turbulence in the remote sensing era (1979–2018). *Remote Sens.*, **16**, 2038, https://doi.org/10.3390/rs16112038.

Salzmann, M., 2017: The polar amplification asymmetry: Role of Antarctic surface height. *Earth Syst. Dyn.*, **8**, 323–336, https://doi.org/10.5194/esd-8-323-2017.

Santer, B. D., and Coauthors, 2005: Amplification of surface temperature trends and variability in the tropical atmosphere. *Science*, **309**, 1551–1556, https://doi.org/10.1126/science.1114867.

Shapiro, M. A., 1980: Turbulent mixing within tropopause folds as a mechanism for the exchange of chemical constituents between the stratosphere and troposphere. *J. Atmos. Sci.*, **37**, 994–1004, https://doi.org/10.1175/1520-0469(1980)037<0994:TMWTFA>2.0.CO;2.

Sharman, R., and T. Lane, 2016: *Aviation Turbulence: Processes, Detection, Prediction.* Springer, 316 pp.

——, and J. M. Pearson, 2017: Prediction of energy dissipation rates for aviation turbulence. Part I: Forecasting nonconvective turbulence. *J. Appl. Meteor. Climatol.*, **56**, 317–337, https://doi.org/10.1175/JAMC-D-16-0205.1.

——, C. Tebaldi, G. Wiener, and J. Wolff, 2006: An integrated approach to mid- and upper-level turbulence forecasting. *Wea. Forecasting*, **21**, 268–287, https://doi.org/10.1175/WAF924.1.

——, L. B. Cornman, G. Meymaris, J. Pearson, and T. Farrar, 2014: Description and derived climatologies of automated in situ eddy-dissipation-rate reports of atmospheric turbulence. *J. Appl. Meteor. Climatol.*, **53**, 1416–1432, https://doi.org/10.1175/JAMC-D-13-0329.1.

Shaw, T. A., and O. Miyawaki, 2024: Fast upper-level jet stream winds get faster under climate change. *Nat. Climate Change*, **14**, 61–67, https://doi.org/10.1038/s41558-023-01884-1.

——, and Coauthors, 2016: Storm track processes and the opposing influences of climate change. *Nat. Geosci.*, **9**, 656–664, https://doi.org/10.1038/ngeo2783.

Shepherd, T. G., 2008: Dynamics, stratospheric ozone, and climate change. *Atmos.–Ocean*, **46**, 117–138, https://doi.org/10.3137/ao.460106.

——, 2014: Atmospheric circulation as a source of uncertainty in climate change projections. *Nat. Geosci.*, **7**, 703–708, https://doi.org/10.1038/ngeo2253.

Simmons, A. J., 2022: Trends in the tropospheric general circulation from 1979 to 2022. *Wea. Climate Dyn.*, **3**, 777–809, https://doi.org/10.5194/wcd-3-777-2022.

Simpson, I. R., 2016: Climate change predicted to lengthen transatlantic travel times. *Environ. Res. Lett.*, **11**, 031002, https://doi.org/10.1088/1748-9326/11/3/031002.

Singh, M. S., and P. A. O'Gorman, 2012: Upward shift of the atmospheric general circulation under global warming: Theory and simulations. *J. Climate*, **25**, 8259–8276, https://doi.org/10.1175/JCLI-D-11-00699.1.

Smith, D. M., and Coauthors, 2019: The Polar Amplification Model Intercomparison Project (PAMIP) contribution to CMIP6: Investigating the causes and consequences of polar amplification. *Geosci. Model Dev.*, **12**, 1139–1164, https://doi.org/10.5194/gmd-12-1139-2019.

Smith, I. H., P. D. Williams, and R. Schiemann, 2023: Clear-air turbulence trends over the North Atlantic in high-resolution climate models. *Climate Dyn.*, **61**, 3063–3079 https://doi.org/10.1007/s00382-023-06694-x.

Sridhar, B., H. K. Ng, and N. Y. Chen, 2011: Aircraft trajectory optimization and contrails avoidance in the presence of winds. *J. Guid. Control Dyn.*, **34**, 1577–1584, https://doi.org/10.2514/1.53378.

Stohl, A., and Coauthors, 2003: Stratosphere-troposphere exchange: A review, and what we have learned from STACCATO. *J. Geophys. Res.*, **108**, 8516, https://doi.org/10.1029/2002JD002490.

——, O. R. Cooper, and P. James, 2004: A cautionary note on the use of meteorological analysis fields for quantifying atmospheric mixing. *J. Atmos. Sci.*, **61**, 1446–1453, https://doi.org/10.1175/1520-0469(2004)061<1446:ACNOTU>2.0.CO;2.

Storer, L. N., P. D. Williams, and M. M. Joshi, 2017: Global response of clear-air turbulence to climate change. *Geophys. Res. Lett.*, **44**, 9976–9984, https://doi.org/10.1002/2017GL074618.

Strong, C., and R. E. Davis, 2007: Winter jet stream trends over the Northern Hemisphere. *Quart. J. Roy. Meteor. Soc.*, **133**, 2109–2115, https://doi.org/10.1002/qj.171.

Stuecker, M. F., and Coauthors, 2018: Polar amplification dominated by local forcing and feedbacks. *Nat. Climate Change*, **8**, 1076–1081, https://doi.org/10.1038/s41558-018-0339-y.

Swart, N. C., S. T. Gille, J. C. Fyfe, and N. P. Gillett, 2018: Recent Southern Ocean warming and freshening driven by greenhouse gas emissions and ozone depletion. *Nat. Geosci.*, **11**, 836–841 https://doi.org/10.1038/s41561-018-0226-1.

Trenberth, K. E., and D. P. Stepaniak, 2003: Seamless poleward atmospheric energy transports and implications for the Hadley circulation. *J. Climate*, **16**, 3706–3722, https://doi.org/10.1175/1520-0442(2003)016<3706:SPAETA>2.0.CO;2.

Trier, S. B., R. D. Sharman, D. Muñoz-Esparza, and T. L. Keller, 2022: Effects of distant organized convection on forecasts of widespread clear-air turbulence. *Mon. Wea. Rev.*, **150**, 2593–2615, https://doi.org/10.1175/MWR-D-22-0077.1.

Vallis, G. K., P. Zurita-Gotor, C. Cairns, and J. Kidston, 2015: Response of the large-scale structure of the atmosphere to global warming. *Quart. J. Roy. Meteor. Soc.*, **141**, 1479–1501, https://doi.org/10.1002/qj.2456.

Vecchi, G. A., and B. J. Soden, 2007: Global warming and the weakening of the tropical circulation. *J. Climate*, **20**, 4316–4340, https://doi.org/10.1175/JCLI4258.1.

Wallace, J. M., and P. V. Hobbs, 2006: *Atmospheric Science: An Introductory Survey*. Academic Press, 488 pp.

Wang, Z., 2013: On the response of Southern Hemisphere subpolar gyres to climate change in coupled climate models. *J. Geophys. Res. Oceans*, **118**, 1070–1086, https://doi.org/10.1002/jgrc.20111.

Williams, P. D., 2016: Transatlantic flight times and climate change. *Environ. Res. Lett.*, **11**, 024008, https://doi.org/10.1088/1748-9326/11/2/024008.

——, 2017: Increased light, moderate, and severe clear-air turbulence in response to climate change. *Adv. Atmos. Sci.*, **34**, 576–586, https://doi.org/10.1007/s00376-017-6268-2.

——, and M. M. Joshi, 2013: Intensification of winter transatlantic aviation turbulence in response to climate change. *Nat. Climate Change*, **3**, 644–648, https://doi.org/10.1038/nclimate1866.

——, and L. N. Storer, 2022: Can a climate model successfully diagnose clear-air turbulence and its response to climate change? *Quart. J. Roy. Meteor. Soc.*, **148**, 1424–1438, https://doi.org/10.1002/qj.4270.

Woollings, T., J. M. Gregory, J. G. Pinto, M. Reyers, and D. J. Brayshaw, 2012: Response of the North Atlantic storm track to climate change shaped by ocean–atmosphere coupling. *Nat. Geosci.*, **5**, 313–317, https://doi.org/10.1038/ngeo1438.

Wu, G., Y. Liu, B. He, Q. Bao, A. Duan, and F.-F. Jin, 2012: Thermal controls on the Asian summer monsoon. *Sci. Rep.*, **2**, 404, https://doi.org/10.1038/srep00404.

Yeung, N. K.-H., L. Menviel, K. J. Meissner, A. S. Taschetto, T. Ziehn, and M. Chamberlain, 2021: Land–sea temperature contrasts at the last interglacial and their impact on the hydrological cycle. *Climate Past*, **17**, 869–885, https://doi.org/10.5194/cp-17-869-2021.

Yin, J. H., 2005: A consistent poleward shift of the storm tracks in simulations of 21st century climate. *Geophys. Res. Lett.*, **32**, L18701, https://doi.org/10.1029/2005GL023684.

Zeng, Z., S. Yang, Z. Wang, H. Luo, and K. Deng, 2024: Weakened subtropical westerlies and their deflection by the Tibetan Plateau contribute to drying southeastern China in early spring. *Geophys. Res. Lett.*, **51**, e2024GL109795, https://doi.org/10.1029/2024GL109795.

Zhu, J., A. Xie, X. Qin, B. Xu, and Y. Wang, 2023: Assessment of Antarctic amplification based on a reconstruction of near-surface air temperature. *Atmosphere*, **14**, 218, https://doi.org/10.3390/atmos14020218.